

1 **Polarization properties of aerosol particles over western Japan:** 2 **Classification, seasonal variation, and implications for air quality**

3
4 **X.L. Pan^{1,2}, I. Uno², Y. Hara², K. Osada³, S. Yamamoto⁴, Z. Wang^{2,1}, N. Sugimoto⁵, H.**
5 **Kobayashi⁶ and Z.F. Wang¹**

6 [1] Institute of Atmospheric Physics, Chinese Academy of Sciences, Beijing, China

7 [2] Research Institute for Applied Mechanics, Kyushu University, Kasuga, Japan

8 [3] Graduate School of Environmental Studies, Nagoya University, Nagoya, Japan

9 [4] Fukuoka Institute of Health and Environmental Sciences, Daizaifu, Japan

10 [5] National Institute for Environmental Studies, Ibaraki, Japan

11 [6] University of Yamanashi, Yamanashi, Japan

12 Corresponding author: X.L. Pan (panxiaole@mail.iap.ac.cn)

13 14 **Abstract**

15 Ground-based observation of the polarization properties of aerosol particles using a
16 polarization optical particle counter (POPC) was made from October 27, 2013, to December
17 31, 2015, at a suburban site in the Kyushu area of Japan. We found that the depolarization
18 ratio (DR, the fraction of s-polarized signal in the total backward light scattering signal) of
19 aerosol particles showed prominent seasonal variability, with peaks in spring (0.21–0.23) and
20 winter (0.19–0.23), and a minimum value (0.09–0.14) in summer. The aerosol compositions
21 in both fine mode (aerodynamic diameter of particle, $D_p < 2.5 \mu\text{m}$) and coarse mode ($2.5 \mu\text{m}$
22 $< D_p < 10 \mu\text{m}$), and the size-dependent polarization characteristics were analyzed for long-
23 range-transport dust particles, sea salt, and anthropogenic pollution-dominant aerosols. The
24 DR value increased with increasing particle size, and $\text{DR} = 0.1$ was a reliable threshold value
25 to identify the sphericity of supermicron ($D_p > 1 \mu\text{m}$) particles. Occurrence of substandard air
26 quality days in Kyushu was closely related with mixing type (coexistence of anthropogenic
27 pollutants and dust particles in the atmosphere), especially in winter and spring, indicating
28 that dust events in the Asian continent played a key role in the cross-boundary transport of
29 continental pollution. Backward trajectory analysis demonstrated that air masses originating
30 from the western Pacific contained large amounts of spherical particles due to the influence
31 of sea salt, especially in summer; however, for air masses from the Asian continent, the
32 dependence of number fraction of spherical particles on air relative humidity was
33 insignificant, indicating the predominance of less-hygroscopic substances (e.g., mineral dust),

34 although the mass concentrations of anthropogenic pollutants were elevated.

35 **1. Introduction**

36 The East Asian region is characterized by serious regional anthropogenic pollution, due to the
37 mass consumption of fossil fuel in China (Kurokawa *et al.*, 2013). The region is also
38 influenced by sporadic occurrences of dust plumes from the Taklimakan/Gobi Desert (Uno *et al.*,
39 *et al.*, 2009, Yumimoto *et al.*, 2009). The environmental/climate effects of these anthropogenic
40 and mineral dust aerosols are notably different because of their distinct chemical and physical
41 properties, size distributions, and lifetimes in the troposphere (Pan *et al.*, 2009). Dust aerosols
42 can trap substantial amounts of pollutants (e.g., nitrate), forming a so-called “polluted dust”
43 when they are transported through the planetary boundary layer (PBL) of polluted areas
44 (Wang *et al.*, 2002, Zhang *et al.*, 2005, Zhang *et al.*, 2006). As a consequence, there is
45 substantial variability in their resulting hygroscopic properties, which contributes to
46 considerable uncertainty in predicting their climate effects with models. The light
47 polarization property of a particle is a good proxy indicator of its sphericity/non-sphericity.
48 As such, ground-based light detection and ranging (Lidar) and Cloud-Aerosol Lidar with
49 Orthogonal Polarization (CALIOP) have been developed to derive the attenuated
50 backscattering coefficient at 1064 nm and 532 nm and volume depolarization ratio at 532 nm,
51 the latter of which was used to investigate the temporal and spatial characteristics of dust and
52 pollutant particles in the atmosphere (Shimizu *et al.*, 2004, Winker *et al.*, 2009, Sugimoto and
53 Huang, 2014, Sugimoto *et al.*, 2015). These can be used to investigate the mixing state of
54 dust particles because the data points of pure dust particles are normally in the upper-right
55 portion of a depolarization versus backscattering ratio (1064 nm/532 nm) plot, clearly
56 separate from the data points of pollutant aerosols (in the lower-left portion), with data to the
57 right side of the line connecting the two data clusters reflecting the variation of the mixing
58 state of particles (Sugimoto *et al.*, 2002). Theoretically, the particles with a smaller
59 depolarization ratio (DR, the fraction of *s*-polarized to the total backward scattering,
60 $[S/(S+P)]$) and larger backscattering color ratio may be related to internally mixed Asian
61 dusts; however, this cannot be confidently concluded because the external mixture of dust
62 and large spherical particles (e.g., sea salt) has a similar pattern on the basis of volume
63 backscattering measurements by lidar (Sugimoto *et al.*, 2015).

64 Recently, a bench-top optical particle counter equipped with a depolarization module was
65 developed. The major advantage of this instrument is its ability to depict the size-resolved
66 polarization of particles (Kobayashi *et al.*, 2014), providing the potential to quantitatively
67 investigate the evolution of the mixing of dust particles during their transport. A study in
68 Seoul (Longitude: 128.95E, Latitude: 37.46N, 116 m a.s.l.) reported the internal mixing of

69 Asian dust with anthropogenic pollutants on the basis of an evident decrease in the
70 backscattering DR of all particles during a polluted dust episode (Sugimoto *et al.*, 2015). The
71 observation (Pan *et al.*, 2015) of a 7-day dust event in Kyushu in 2014 found that the size-
72 dependent polarization property of particles varied significantly throughout the dust event,
73 and the decrease in the DR of supermicron (aerodynamic diameter of particle, $D_p > 1 \mu\text{m}$)
74 particles was mostly due to an increase in the coarse mode nitrate concentration. This
75 phenomenon was verified by an off-line analysis with transmission electron microscopy (Li
76 and Shao 2009, Li *et al.*, 2011) and a model simulation, which highlighted the direct
77 absorption of nitric acid gas by the dust surface, and/or the volatilization of ammonium
78 nitrate particulate as well as the resulting transfer of nitrate to the dust due to heterogeneous
79 reactions during transport (Allen *et al.*, 2015).

80 To determine the mixing state of dust particles outflowing from the Asian continent, a long-
81 term field observation was performed at a suburban site in Fukuoka, on the westernmost edge
82 of Japan, beginning in October 2013. The geographic location of the observation site is
83 shown in Figure 1. This location is subject to long-range transport of both anthropogenic
84 pollutions and dust plumes from the Asian continent in spring. Although local emissions (e.g.,
85 NO_x) contribute to the nitrate mass, transport is largely responsible for the buildup of $\text{PM}_{2.5}$
86 (particulate matter with a diameter less than or equal to $2.5 \mu\text{m}$) in this city (Kaneyasu *et al.*,
87 2014), particularly during the late winter-spring period. In this study, size-dependent
88 polarization characteristics for single particles were continuously measured by a polarization
89 optical particle counter (POPC), and three common aerosol types (anthropogenic pollutants,
90 dust, and sea salt) were classified, together with an analysis of some key pollutant parameters
91 (sulfate, nitrate, particulate acidity, etc.). The contributions of different aerosol types to
92 ambient aerosol concentrations were investigated. The sphericity/non-sphericity of aerosols
93 from different origins, their relative humidity (RH) dependence, and corresponding impacts
94 on the local air quality in Fukuoka city were investigated using a combined ensemble
95 backward trajectory analysis.

96 **2. Measurements**

97 The light polarization properties of atmospheric aerosol particles ($0.5 \mu\text{m} < D_p < 10 \mu\text{m}$) were
98 measured using a newly developed POPC (YGK Corp., Yamanashi, Japan) at the top of a
99 two-story building at Kyushu University (Longitude: 130.5°E , Latitude: 33.5°N) in Fukuoka
100 prefecture, Japan. We installed a 3 m long vertical stainless steel tube through the roof of the
101 building, and ambient air was drawn into the room with a laminar flow rate of 13 L/min. The
102 loss of coarse mode particles ($D_p > 2.5 \mu\text{m}$) due to gravity settling was negligible. The
103 detailed set-up of the instrumentation is shown in Figure 2. The POPC uses a 780 nm linearly

104 polarized laser source, and measures both forward scattering and backward scattering
105 intensities at 60 degrees and 120 degrees, relative to the direction of incident light. The
106 polarization direction of the incident laser is parallel to the plane of the scattering angle, and
107 the acceptance angle for the polarization detector is 45 degrees (Kobayashi *et al.*, 2014). The
108 sampling rate and half-width of full height (WHFH) of the POPC detector's output signal
109 were 2×10^6 samples/s and ~ 35 μ s, respectively. During the measurements, the pulse signals
110 were sampled during 1 s and processed for 1.2 s. The size of particles is determined from the
111 forward scattering intensity, and two polarized compounds (*s*-polarized/*p*-polarized,
112 polarization direction perpendicular/parallel to the plane of the scattering angle) of backward
113 scattering are measured simultaneously. In practice, the DR is a good indicator of particle
114 sphericity because the direction of polarization of scattered light for spherical particles is
115 identical to that of the incident light, while this is not the case for non-spherical particles (e.g.,
116 dust). The DR thresholds for determining the sphericity/non-sphericity of particles are not
117 uniform for different optical instrumentations. For example, lidar observations classify
118 aerosols on the basis of an empirically determined aerosol back-scattering DR ($\delta_a = S/P$), and
119 the values of $\delta_a < 0.02$ and $\delta_a > 0.35$ (DR = 0.03, 0.26, respectively in this context) are
120 regarded as the thresholds for pure spherical and non-spherical dust particles (Shimizu *et al.*,
121 2004). Regarding the use of a POPC, Kobayashi *et al.* (2014) proposed a threshold of
122 DR > 0.2 as being "non-spherical" for supermicron particles (e.g., dust) according to the
123 number concentration of particles measured at Fukuoka University. The POPC was calibrated
124 at the observatory every 6 months. The spherical polystyrene standard (Dynospheres, $D_p =$
125 0.5 μ m, 1 μ m, 3 μ m, 5 μ m, and 10 μ m, JSR Life Sciences Corporation) aerosols were
126 generated by a nebulizer at an injection flow rate of 3.5 liters per minute (Lpm), and
127 desiccated by passing through a 45 cm Perma casing tube (MD-110-24P, GL Sciences). The
128 measurement uncertainty was 10–15%.

129 In this study, mass concentrations of particulate matter (PM), sulfate ion (SO_4^{2-}), nitrate ion
130 (NO_3^-), water-soluble organic compounds (WSOC), and particle acidity ($\text{c}\Delta\text{H}^+$) in both the
131 fine ($D_p < 2.5$ μ m) and coarse mode (2.5 μ m $< D_p < 10$ μ m) were simultaneously measured
132 using a continuous dichotomous Aerosol Chemical Speciation Analyzer (ACSA-12,
133 KIMOTO electric Co. Ltd, Osaka, Japan) at 1 h intervals at the observation site. The mass
134 concentration of PM and SO_4^{2-} were determined using the beta-ray absorption method and the
135 BaSO_4 -based turbidimetric method, respectively, the latter with the addition of BaCl_2
136 dissolved in polyvinylpyrrolidone solution. The mass concentrations of NO_3^- and WSOC
137 were determined with an ultraviolet absorption-photometric method. The $\text{c}\Delta\text{H}^+$ (nmol/m^3),
138 which refers to the difference of the solution of particles relative to the extracting liquid, was

139 determined using a pH-indicator absorption-photometric method. The basic equation is
140 $\text{pH}_{\text{solution}} = -\log [c\Delta\text{H}^+ \times 10^{-6} + 10^{-4.6}]$. Here $\text{pH}_{\text{solution}}$ is the pH value of aqueous extracts of
141 aerosol sample, and the extract solvent had a pH of 4.6. The details of the ACSA instrument
142 have been published elsewhere (Kimoto *et al.*, 2013).

143 3. Results

144 3.1 Temporal variation

145 The daily (00:00–23:00) averaged volume concentration of particles in different aerosol size
146 bins at the observation site are shown in Figure 3a. In general, the volume concentrations of
147 ambient particles had two pronounced peaks in the fine and/or coarse mode size ranges,
148 particularly in spring and winter. The peak in the fine mode was mostly attributed to
149 anthropogenic pollution, while the coarse mode peak (4–8 μm) was related to mineral dust.
150 The two peaks occurred concurrently or sequentially as a result of different prominent
151 outflow patterns. Itahashi *et al.*(2010) reported that dust and pollution were trapped and well
152 mixed within the PBL, when dust events broke out “behind a cold front,” and were
153 characterized by strong stratification. In summer, the volume concentration of particles in
154 both fine and coarse modes decreased significantly because the air masses mostly originated
155 from the western Pacific Ocean where anthropogenic emissions were limited. Wet
156 scavenging processes were significant during summer in Kyushu. The 1 h averaged DR
157 values of particles in each size range during the observation period are shown in Figure 3b.
158 DR value showed a marked increase with increase in particle size, and the dust-impacting
159 episode at the site could be easily identified owing to the distinct increase in the DR value of
160 particles in the fine mode. Due to the clear influence of long-range transport mineral dust at
161 the site, monthly averaged DR values of aerosols in fine mode showed a marked seasonality,
162 with a maximum (~ 0.14) in spring and minimum (~ 0.09) in summer (Figure 3c).

163 3.2 Size distribution

164 The normalized volume size distribution ($dV/d\log D_p$) of aerosol particles at the site showed
165 prominent seasonal variation (Figure 4). The averaged DR values of each season at the peak
166 size are shown as red circles in the plot. In spring (March, April, and May: MAM), the
167 $dV/d\log D_p$ of particles had a broad peak between 4 μm and 6 μm due to the impact of
168 frequent outbreaks and transport of Asian dust (Figure 4a). The typical DR value at the peak
169 size was 0.21–0.23. In summer (June, July, and August: JJA) the peak size of $dV/d\log D_p$ was
170 2–3 μm , and the corresponding DR values of particles in the fine mode were less than 0.1.
171 This decrease was mostly due to air masses that originated from clean marine regions and
172 consisted of large amounts of sea salt aerosols, which tend to be spherical under high-

173 humidity conditions. In autumn, the volume concentrations of particles at the site had their
174 minimum values because of less influence from Asian continent during this season and the
175 meteorological conditions were favorable for proliferation of air pollutants. In winter
176 (December, January, and February: DJF), $dV/d\log D_p$ had two peaks in both the submicron
177 range ($D_p = 0.5 \mu\text{m}$) and coarse mode ($D_p = 4 \mu\text{m}$), indicating the combined impact of both
178 anthropogenic pollutants and dust aerosols in the prevailing westerly winds. The DR values at
179 $D_p = 0.5 \mu\text{m}$ and $D_p = 4 \mu\text{m}$ were 0.09 and 0.23, respectively.

180 It was notable that the observed DR values of particles always showed a marked increase
181 with size in all seasons that was almost independent of aerosol types. This trend was well
182 predicted by an optical model considering particles of Voronoi aggregation (SF.1 in
183 Supplementary Information). Theoretical simulation also indicated that an increase in the
184 imaginary part of the refractive index could significantly reduce the DR value; however, from
185 observation, DR values in the coarse mode showed a tendency to increase followed by a
186 leveling off, implying that internal mixing with light-absorbing matter was less important at
187 the site.

188 Calibration of the POPC using DYNOSHERE (JSR Life Sciences Corp.) aerosols yielded DR
189 values of 0.08, 0.09, and 0.1 for pure spherical particles at $D_p = 5 \mu\text{m}$, $7 \mu\text{m}$, and $10 \mu\text{m}$,
190 respectively; and the DR values were almost zero for the particles at $D_p = 1 \mu\text{m}$, $2 \mu\text{m}$, and 3
191 μm . Nevertheless, in this study, the DR values of aerosols in the coarse modes were 0.2–0.28,
192 much larger than calibration results, indicating that these aerosol particles were generally
193 non-spherical, despite the fact that hygroscopic particles (such as sea salt) may deliquesce
194 and grow under very humid conditions.

195 **4 Discussion**

196 **4.1 Size polarization properties for aerosol classification**

197 We classified three distinct aerosol-dominant scenarios based on the mass concentrations of
198 $\text{PM}_{2.5}$ and $\text{PM}_{2.5-10}$ ($2.5 \mu\text{m} < D_p < 10 \mu\text{m}$), and SO_4^{2-} ions in the fine mode ($f\text{SO}_4^{2-}$), and NO_3^-
199 ions in both the fine ($f\text{NO}_3^-$) and coarse modes ($c\text{NO}_3^-$), as shown in Table 1. During
200 anthropogenic pollution-dominant episodes, the mass concentration of $\text{PM}_{2.5}$ was $63.4 \mu\text{g}/\text{m}^3$,
201 which was about five times higher than the $\text{PM}_{2.5-10}$ concentrations ($12.9 \mu\text{g}/\text{m}^3$). The sum of
202 $f\text{SO}_4^{2-}$ and $f\text{NO}_3^-$ ions accounted for 50% of the total $\text{PM}_{2.5}$ mass. During dust-dominant
203 episodes, the mass concentrations of $\text{PM}_{2.5}$ and $\text{PM}_{2.5-10}$ were 25.2 and $58.6 \mu\text{g}/\text{m}^3$,
204 respectively, with minimal contributions from anthropogenic pollutants to the $\text{PM}_{2.5}$ mass
205 ($f\text{SO}_4^{2-} : 1.5 \mu\text{g}/\text{m}^3$; $f\text{NO}_3^- : 2.7 \mu\text{g}/\text{m}^3$). Because we did not measure sodium or chloride ions,
206 a quantitative determination of the influence of sea salt was difficult; however, we could

207 reasonably assume that during the typhoon period, sea salt aerosol was dominant. Detailed
208 information regarding the trajectory of the two typhoons (No. 18 Phanfone and No. 19
209 Vongfong, SF.2 in Supplementary Information) during the study period is provided on the
210 Japan Meteorological Agency webpage
211 (http://www.data.jma.go.jp/fcd/yoho/typhoon/route_map/index.html). The mass
212 concentrations of $PM_{2.5}$, $PM_{2.5-10}$, fSO_4^{2-} , and fNO_3^- were small during the typhoon period
213 with mean values of $5.3 \mu\text{g}/\text{m}^3$, $4.9 \mu\text{g}/\text{m}^3$, $0.4 \mu\text{g}/\text{m}^3$, and $1.5 \mu\text{g}/\text{m}^3$, respectively.

214 To identify the polarization characteristics for the different aerosol types, the volume
215 concentration of particles at different depolarization ratios and particle sizes during specific
216 periods were plotted (Figure 5). To aid comparison, the volume concentration in the plot was
217 normalized to a maximum value = 1 using the equation: $(value - min)/(max - min)$ (hereafter;
218 referred to as a DR- D_p -Volume plot). We divided the plot into four subregions. The plot
219 shows that anthropogenic pollution-dominant aerosols were mostly in the submicron range,
220 with DR values < 0.2 (marked as region “A1,” in Figure 5a). Mineral-dust-dominant aerosols
221 had a larger diameter ($D_p > 4 \mu\text{m}$) and a non-spherical morphology associated with a DR
222 value of 0.4 (marked as region “A2,” in Figure 5b). Sea-salt-dominant aerosols were in the
223 supermicron range, with DR values < 0.1 (marked as region “A3,” in Figure 5c). During the
224 typhoon period, we considered the sea salt particles to be spherical because sea salt occurs as
225 entirely liquid drops when $RH > 75\%$ (Wise *et al.*, 2007). Based on this information, we
226 proposed a DR threshold value of 0.1 to distinguish between spherical and non-spherical
227 particles in the supermicron size range. This criterion was consistent with the theoretical Mie-
228 scattering calculation and classification in the literature (Kobayashi *et al.*, 2014). The
229 sphericity/non-sphericity of submicron particles with $DR > 0.2$ was not considered because of
230 the low volume concentration. With regard to A1, we cannot be specific about the
231 sphericity/non-sphericity of the particles because the morphology of anthropogenic particles
232 is extremely variable, and depends on the mass fractions of carbonaceous matter and water-
233 soluble inorganics, as well as meteorological conditions (e.g., RH), the mixing state, and the
234 degree of atmospheric aging (Li *et al.*, 2011, Fu *et al.*, 2012). Additionally, the *s*-polarized
235 backscattering of submicron particles decreased significantly with a decrease in their size on
236 the basis of theoretical simulations, even for non-spherical particles (Sugimoto *et al.*, 2015).

237 **4.2 Contributions of different aerosol types to local air quality**

238 Using the criteria suggested in Section 4.1, we investigated the impacts of different aerosol
239 types on local air quality in western Japan. The period when the DR- D_p -volume plot had
240 only one prominent volume mode in A1 with mode DR value > 0.1 was considered
241 anthropogenic-pollution-dominant. The dust-dominant period was characterized by a distinct

242 volume mode in “A2” and mode DR value > 0.3 . Periods when three distinct modes occurred
243 simultaneously in A1, A2, and A3 were considered to represent a “mixed type”(Figure 5d).
244 Determination of the sea-salt-dominant period was based on two distinct volume modes in
245 the fine mode, and small DR values (<0.1). A scenario in which the DR- D_p -volume plot had
246 only two volume modes in both A2 and A3 were also observed during a long-lasting dust
247 event at the end of May 2015 (Pan *et al.*, 2015); we considered this “dust dominant.”

248 Monthly-averaged and median mass concentrations of $PM_{2.5}$ and $PM_{2.5-10}$ in 2014 and 2015
249 are shown in Figure 6a. In general, ambient $PM_{2.5}$ levels displayed a clear winter-spring high
250 and summer low. In contrast, the mass concentrations of $PM_{2.5-10}$ had a pronounced peak in
251 May, reflecting frequent dust events. The average monthly values were generally larger than
252 the median values during spring, indicating that the observation site was influenced by
253 several intensive pollution events. Figure 6b depicts the number of substandard days that the
254 daily-averaged mass concentration of $PM_{2.5}$ exceeded the National Ambient Air Quality
255 Standard (NAAQS) of Japan ($35 \mu\text{g}/\text{m}^3$) in each month during the observation period. It can
256 be seen that the greatest number of substandard days (12) occurred in May 2014, and mixed
257 type pollutants were responsible for about 60% of these substandard days, followed by dust-
258 dominant types (25%). It is notable that the number of substandard days in a month was
259 closely correlated with the number fraction of “mixed type” pollution during winter and
260 spring. This indicates that air quality in western Japan was influenced mainly by long-range
261 transport of dust and pollution mixed aerosols from the Asian continent. Cross-boundary
262 transport of anthropogenic pollutants during dust events has been reported in several previous
263 studies. The influence of dust-dominant aerosol was generally less than 5% over the course of
264 1 year. Anthropogenic pollution-dominant cases were mostly responsible for substandard
265 days in summer, although only a few such days were observed during the study period.

266 It was notable that the monthly-averaged mass concentrations of $PM_{2.5}$ in winter (23.7 ± 4.3
267 $\mu\text{g}/\text{m}^3$) and spring ($27 \pm 3.8 \mu\text{g}/\text{m}^3$) of 2014 were greater than those ($20.9 \pm 1.9 \mu\text{g}/\text{m}^3$ and
268 $20.4 \pm 1.5 \mu\text{g}/\text{m}^3$) in 2015, and that the number of substandard days in 2014 was also higher
269 than that in 2015. This implies that transport from the Asian continent was relatively
270 intensive in 2014. The causes of this difference in variation in regional synoptic weather
271 conditions and emissions inventories provide important topics for future studies.

272 **4.3 Polarization properties of aerosols from different origins**

273 The DR- D_p -volume plots of aerosol particles from different geographical origins were
274 evaluated in combination with a backward trajectory analysis (Figure 7). The footprint
275 regions for air masses were determined based on ensemble simulations of 5-day backward

276 trajectories of air parcels using the Hybrid Single Particle Lagrangian Integrated Trajectory
277 (HYSPLIT) model (v4.9; available at <http://ready.arl.noaa.gov/HYSPLIT.php>), offsetting the
278 release point by a meteorological grid point in the horizontal and 0.01 sigma units in the
279 vertical. Therefore 27 trajectories were calculated simultaneously in each hour. We divided
280 the region of interest into four sub-regions, where the emission intensity of pollutants and
281 aerosol types were different. In Region I (Figure 7a), which mostly covered the Japanese
282 landmass, the DR- D_p -volume plot had one predominant peak at MDR = 0.05 and D_p = 1.8
283 μm (Figure 7b). The small polarization degree of aerosol particles in the fine mode indicated
284 that the aerosol particles tended to be spherical. Only 2% of this period was found to have
285 substandard air quality. When the air mass came from Region II which included the polluted
286 region of northern China and the Korean Peninsula (Figure 7c) the volume concentrations of
287 particles in all size bins increased significantly, and the volume size distributions of particles
288 had three distinct modes at D_p = 0.7 μm (MDR = 0.1), D_p = 1.9 μm (MDR = 0.08), and D_p =
289 5 μm (MDR = 0.35) (Figure 7d). The volume peaks in the coarse modes could be attributed to
290 long-range transport of mineral dust. We found that 32% of the days, dominated by
291 northwesterly winds, were substandard, i.e., anthropogenic-pollutant-dominant, mineral-dust-
292 dominant, and mixed-type-dominant aerosols contributed to 13%, 8%, and 11% of period,
293 respectively. When air masses came from Region III (East China Sea, Figure 7e), 92% of
294 these days met the NAAQS for Japan, and substandard days were mostly related to
295 anthropogenic pollution (9%). The MDR (0.03) for supermicron particles was very small
296 (Figure 7f), indicating a high degree of sphericity. Air masses from Region VI (western
297 Pacific Ocean, Figure 7g) also contained a large volume fraction of supermicron particles,
298 with small MDR values (~ 0.03). We found that substandard air quality days (16% of all days),
299 when air masses came from Region VI, were more frequent than for Region III, reflecting the
300 mixing of maritime air with local anthropogenic emissions over the western part of Japan
301 (Figure 7g). It should be noted that the air masses arriving from different regions displayed
302 distinct seasonality (Table 2), and that the acidities of particles in the coarse mode ($c\Delta\text{H}^+$)
303 showed a marked difference. Air masses from Region I were concentrated in summer and
304 autumn ($c\Delta\text{H}^+ = 3.6 \pm 1.4 \text{ nmol/m}^3$). Air masses from Region II occurred more frequently in
305 winter ($c\Delta\text{H}^+ = -4.7 \pm 1.0 \text{ nmol/m}^3$) and spring ($c\Delta\text{H}^+ = -2.8 \pm 1.0 \text{ nmol/m}^3$), and the negative
306 $c\Delta\text{H}^+$ indicated that the air masses contained of alkaline substances (Ca^{2+} , Mg^{2+} etc.) Air
307 masses from Region III ($c\Delta\text{H}^+ = 2.0 \pm 3.0 \text{ nmol/m}^3$) and Region IV ($c\Delta\text{H}^+ = 7.5 \pm 4.9$
308 nmol/m^3) occurred only in summer. Overall, the DR- D_p -volume plots in Figure 8 provide an
309 accurate representation of the polarization characteristics of particles from different regions.

310 4.4 Fraction of spherical particles as a function of RH

311 As mentioned in previous studies (Koehler *et al.*, 2009, Sullivan *et al.*, 2009), the more dust
312 particles become involved in chemical mixing, the more easily they become hydrophilic and
313 are incorporated into cloud processes, which results in complicated climate effects. Here, the
314 hygroscopicity of aerosol particles from different regions was investigated on the basis of the
315 number fraction of particles with DR < 0.1 (referred to as “NFP_{DR<0.1}”) as a function of the
316 averaged RH, which was calculated along 3-day backward trajectories (Figure 8). The dataset
317 period when intensive precipitation (>20 mm/hr) occurred along the trajectories was removed.
318 The averaged RH of air masses from Regions III and IV were relatively high (>70%) because
319 of their longer stagnancy in the marine area. For particles with $1.0 < D_p < 1.5 \mu\text{m}$ (Figure 8a),
320 the NFP_{DR<0.1} was positively correlated with the RH for particles from all origins. This
321 phenomenon can be explained by the coexistence of hygroscopic masses such as sulfate and
322 nitrate. About 70% of particles were probably spherical in the air mass from Region I, and
323 this figure increased to 89% at RH = 76%. In the air masses from Region II, NFP_{DR<0.1} was
324 62% at RH = 45% and increased slightly to 72% at RH = 82%. For coarse-mode particles
325 (Figure 8b) from Region II, the NFP_{DR<0.1} was ~32%, irrespective of RH. The chemical
326 analysis indicated that the mass fraction of water-soluble matter in coarse-mode particles
327 ($\text{WSM} = c\text{SO}_4^{2-} + c\text{NO}_3^- + c\text{WSOC}$) from Region II was 15%, similar to that of air masses
328 from other origins. The missing part in mass balance was likely to be related to crustal
329 species (Pan *et al.*, 2009). When the air mass came from Region II, in about 78% of
330 trajectories the acidities of particles were negative with a mean of $-4.4 \pm 3.1 \text{ nmol/m}^3$,
331 indicating that the particles contained of crustal substances. $c\Delta\text{H}^+$ values of particles from
332 other regions were normally positive (as shown in Table 2). This difference also partially
333 explains the weaker hygroscopicity of particles from Region II compared to other regions.
334 The NFP_{DR<0.1} from Regions I and III were still very sensitive to the variation in RH, which
335 suggested that the large aerosol particles were related to hygroscopic aerosols.

336

337 **5 Conclusions**

338 We conducted continuous observations of the polarization properties and chemical
339 composition of aerosol particles in Kyushu during 2014–2015, using a POPC and ACSA-12.
340 The conclusions are as follows: (1) POPC could objectively identify anthropogenic-pollutant-
341 dominant, mineral-dust-dominant, and sea-salt-dominant aerosol types from their distinct
342 depolarization ratio-size characteristics. We suggest that a DR of 0.1 is a reliable threshold
343 that can be used to classify the sphericity/non-sphericity of supermicron particles. (2) We
344 found that LRT dust and pollution mixed events were mainly responsible for substandard air
345 quality days in western Japan in spring and winter. In summer, coarse-mode particle at the

346 observation site were mostly spherical due to the impact of sea salt at high RH conditions. (3)
347 The correlation between the number fraction of spherical particles with DR <0.1 ($NFP_{DR<0.1}$)
348 and RH for coarse-mode particles from Region II was not significant because of the existence
349 of non-hydrophilic materials (i.e., dust). Nevertheless, there was a clear positive correlation
350 between $NFP_{DR<0.1}$ and RH for particles from Regions III and IV, implying a significant
351 impact of sea salt. (4) Local emissions were partially responsible for the occurrence of
352 substandard air quality days in Kyushu, occurring mainly in summer.

353 **Acknowledgments**

354 This work was supported by a Grant-in-Aid for Scientific Research (25220101) from the
355 Japan Society for the Promotion of Science (JSPS). To request POPC data for scientific
356 research purposes, please contact Prof. Itsushi Uno at Kyushu University via email
357 (uno@riam.kyushu-u.ac.jp).

358

359 References

- 360 Allen H. M., Draper D. C., Ayres B. R., Ault A., Bondy A., Takahama S., Modini R. L., Baumann K., Edgerton
361 E., Knote C. Influence of crustal dust and sea spray supermicron particle concentrations and acidity on inorganic
362 NO₃- aerosol during the 2013 Southern Oxidant and Aerosol Study. *Atmospheric Chemistry and Physics*.
363 15(18):10669-85, 2015.
- 364 Dubovik O., Sinyuk A., Lapyonok T., Holben B. N., Mishchenko M., Yang P., Eck T. F., Volten H., Munoz O.,
365 Veihelmann B. Application of spheroid models to account for aerosol particle nonsphericity in remote sensing
366 of desert dust. *Journal of Geophysical Research: Atmospheres* (1984–2012). 111(D11), 2006.
- 367 Fu H., Zhang M., Li W., Chen J., Wang L., Quan X., Wang W. Morphology, composition and mixing state of
368 individual carbonaceous aerosol in urban Shanghai. *Atmospheric Chemistry and Physics*. 12(2):693-707, 2012.
- 369 Itahashi S., Yumimoto K., Uno I., Eguchi K., Takemura T., Hara Y., Shimizu A., Sugimoto N., Liu Z. Structure
370 of dust and air pollutant outflow over East Asia in the spring. *Geophysical Research Letters*. 37(20), 2010.
- 371 Kaneyasu N., Yamamoto S., Sato K., Takami A., Hayashi M., Hara K., Kawamoto K., Okuda T., Hatakeyama
372 S. Impact of long-range transport of aerosols on the PM_{2.5} composition at a major metropolitan area in the
373 northern Kyushu area of Japan. *Atmospheric Environment*.416-25, 2014.
- 374 Kimoto H., Ueda A., Tsujimoto K., Mitani Y., Toyazaki Y., Kimoto T. Development of a Continuous
375 Dichotomous Aerosol Chemical Speciation Analyzer. *Clean Technology*. 23:49-52, 2013.
- 376 Kobayashi H., Hayashi M., Shiraishi K., Nakura Y., Enomoto T., Miura K., Takahashi H., Igarashi Y., Naoe H.,
377 Kaneyasu N. Development of a polarization optical particle counter capable of aerosol type classification.
378 *Atmospheric Environment*.486-92, 2014.
- 379 Koehler K. A., Kreidenweis S. M., DeMott P. J., Petters M. D., Prenni A. J., Carrico C. M. Hygroscopicity and
380 cloud droplet activation of mineral dust aerosol. *Geophysical Research Letters*. 36(8), 2009.
- 381 Kurokawa J., Ohara T., Morikawa T., Hanayama S., Janssens-Maenhout G., Fukui T., Kawashima K., Akimoto
382 H. Emissions of air pollutants and greenhouse gases over Asian regions during 2000–2008: Regional Emission
383 inventory in ASia (REAS) version 2. *Atmospheric Chemistry and Physics*. 13(21):11019-58, 2013.
- 384 Li W. J., Shao L. Y. Observation of nitrate coatings on atmospheric mineral dust particles. *Atmospheric
385 Chemistry and Physics*. 9(6):1863-71, 2009.
- 386 Li W. J., Zhang D. Z., Shao L. Y., Zhou S. Z., Wang W. X. Individual particle analysis of aerosols collected
387 under haze and non-haze conditions at a high-elevation mountain site in the North China plain. *Atmospheric
388 Chemistry and Physics*. 11(22):11733-44, 2011.
- 389 Pan X. L., Uno I., Hara Y., Kuribayashi M., Kobayashi H., Sugimoto N., Yamamoto S., Shimohara T., Wang Z.
390 Observation of the simultaneous transport of Asian mineral dust aerosols with anthropogenic pollutants using a
391 polarization optical particle counter (POPC) during a long-lasting dust event in late spring 2014. *Geophysical
392 Research Letters*.2014GL062491, 2015. 10.1002/2014GL062491, 2015
- 393 Pan X. L., Yan P., Tang J., Ma J. Z., Wang Z. F., Gbaguidi A., Sun Y. L. Observational study of influence of
394 aerosol hygroscopic growth on scattering coefficient over rural area near Beijing mega-city. *Atmospheric
395 Chemistry and Physics*. 9(19):7519-30, 2009.
- 396 Shimizu A., Sugimoto N., Matsui I., Arai K., Uno I., Murayama T., Kagawa N., Aoki K., Uchiyama A.,
397 Yamazaki A. Continuous observations of Asian dust and other aerosols by polarization lidars in China and
398 Japan during ACE-Asia. *Journal of Geophysical Research: Atmospheres* (1984–2012). 109(D19), 2004.
- 399 Sugimoto N., Huang Z. Lidar methods for observing mineral dust. *Journal of Meteorological Research*.
400 28(2):173-84, 2014.
- 401 Sugimoto N., Matsui I., Shimizu A., Uno I., Asai K., Endoh T., Nakajima T. Observation of dust and
402 anthropogenic aerosol plumes in the northwest Pacific with a two-wavelength polarization lidar on board the
403 research vessel Mirai. *Geophysical Research Letters*. 29(19):7-1-7-4, 2002.
- 404 Sugimoto N., Nishizawa T., Shimizu A., Matsui I., Kobayashi H. Detection of internally mixed Asian dust with
405 air pollution Aerosols using a polarization optical particle counter and a polarization-sensitive two-wavelength
406 lidar. *Journal of Quantitative Spectroscopy and Radiative Transfer*. 150:107-13, 2015.
407 10.1016/j.jqsrt.2014.08.003
- 408 Sullivan R. C., Moore M. J. K., Petters M. D., Kreidenweis S. M., Roberts G. C., Prather K. A. Effect of
409 chemical mixing state on the hygroscopicity and cloud nucleation properties of calcium mineral dust particles.
410 *Atmospheric Chemistry and Physics*. 9(10):3303-16, 2009.

411 Tobo Y., Zhang D., Matsuki A., Iwasaka Y. Asian dust particles converted into aqueous droplets under remote
412 marine atmospheric conditions. *Proceedings of the National Academy of Sciences*. 107(42):17905-10, 2010.

413 Uno I., Eguchi K., Yumimoto K., Takemura T., Shimizu A., Uematsu M., Liu Z., Wang Z., Hara Y., Sugimoto
414 N. Asian dust transported one full circuit around the globe. *Nature Geoscience*. 2(8):557-60, 2009.

415 Wang Z., Akimoto H., Uno I. Neutralization of soil aerosol and its impact on the distribution of acid rain over
416 east Asia: Observations and model results. *Journal of Geophysical Research: Atmospheres* (1984–2012).
417 107(D19):ACH 6-1-ACH 6-12, 2002.

418 Winker D. M., Vaughan M. A., Omar A., Hu Y., Powell K. A., Liu Z., Hunt W. H., Young S. A. Overview of
419 the CALIPSO mission and CALIOP data processing algorithms. *Journal of Atmospheric and Oceanic*
420 *Technology*. 26(11):2310-23, 2009.

421 Wise M. E., Semeniuk T. A., Bruintjes R., Martin S. T., Russell L. M., Buseck P. R. Hygroscopic behavior of
422 NaCl-bearing natural aerosol particles using environmental transmission electron microscopy. *Journal of*
423 *Geophysical Research: Atmospheres* (1984–2012). 112(D10), 2007.

424 Yumimoto K., Eguchi K., Uno I., Takemura T., Liu Z., Shimizu A., Sugimoto N. An elevated large-scale dust
425 veil from the Taklimakan Desert: Intercontinental transport and three-dimensional structure as captured by
426 CALIPSO and regional and global models. *Atmospheric Chemistry and Physics*. 9(21):8545-58, 2009.

427 Zhang D., Iwasaka Y., Matsuki A., Ueno K., Matsuzaki T. Coarse and accumulation mode particles associated
428 with Asian dust in southwestern Japan. *Atmospheric Environment*. 40(7):1205-15, 2006.

429 Zhang D., Iwasaka Y., Shi G., Zang J., Hu M., Li C. Separated status of the natural dust plume and polluted air
430 masses in an Asian dust storm event at coastal areas of China. *Journal of Geophysical Research: Atmospheres*
431 (1984–2012). 110(D6), 2005.
432

434 Table 1. Statistics for the mass concentrations of $PM_{2.5}$, $PM_{2.5-10}$, fSO_4^{2-} , fNO_3^- , and cNO_3^- for
 435 three distinct aerosol-dominant periods.

Classification	Date Time	$PM_{2.5}$	$PM_{2.5-10}$	fSO_4^{2-}	fNO_3^-	cNO_3^-
Anthropogenic-pollution-dominant period (n = 12)	2014-01-12 19:00	71.7	16.9	11.5	18.0	3.5
	2014-01-13 01:00	63.6	13.1	10.5	18.9	2.6
	2014-01-13 03:00	61.0	11.8	10.4	17.7	2.9
	2014-01-13 07:00	56.3	11.9	10.0	17.7	2.7
	2014-01-13 10:00	60.4	13.1	10.5	16.2	2.6
	2014-01-17 20:00	61.5	16.2	12.1	17.0	3.1
	2014-01-17 21:00	62.3	13.5	12.0	16.4	3.1
	2014-01-18 03:00	52.4	11.4	11.1	17.0	2.4
	2014-01-18 06:00	56.4	10.8	11.8	19.3	2.5
	2014-01-18 11:00	68.7	13.2	12.7	15.3	3.0
	2014-01-20 18:00	74.5	11.0	15.2	16.8	3.1
	2014-01-26 03:00	72.3	11.9	10.6	16.2	2.6
Average		63.4	12.9	11.5	17.2	2.8
Standard deviation		7.0	1.9	1.4	1.2	0.3
Mineral-dust-dominant period (n=8)	2014-01-01 17:00	22.4	55.4	2.2	2.8	3.8
	2014-01-01 18:00	23.8	52.2	1.9	2.4	2.7
	2014-01-01 21:00	25.6	51.4	1.8	2.9	2.4
	2014-05-18 10:00	25.7	54.5	1.2	2.8	1.6
	2014-05-18 11:00	23.9	63.1	0.9	2.5	1.4
	2014-05-18 12:00	30.0	74.7	1.2	2.7	1.4
	2014-05-18 13:00	35.8	81.3	1.2	3.0	1.6
	Average		25.2	58.6	1.5	2.7
Standard deviation		2.6	8.9	0.5	0.2	0.9
Typhoon period (n=13)	2014-10-05 03:00	6.8	9.4	0.5	1.6	0.5
	2014-10-05 05:00	7.4	8.4	0.5	1.1	0.4
	2014-10-05 06:00	7.2	9.8	0.6	1.3	0.4
	2014-10-05 08:00	7.6	9.0	0.6	1.7	0.4
	2014-10-05 09:00	6.6	8.6	0.6	2.0	0.5
	2014-10-13 02:00	6.2	3.3	0.5	2.5	0.3
	2014-10-13 03:00	5.0	1.8	0.5	2.4	0.3
	2014-10-13 04:00	5.7	3.6	0.3	1.8	0.4
	2014-10-13 05:00	4.5	2.6	0.4	0.9	0.6
	2014-10-13 06:00	2.9	1.5	0.3	1.0	0.8
	2014-10-13 07:00	1.8	0.3	0.3	0.3	0.4
	2014-10-13 08:00	1.5	1.0	0.3	0.9	0.3
	2014-10-13 09:00	2.6	0.1	0.2	0.5	0.2
Average		5.3	4.9	0.4	1.5	0.4
Standard deviation		2.2	3.7	0.1	0.7	0.1

437 Table 2. Number counts of trajectories used in Figure 7 and corresponding monthly averaged
 438 acidities of particles ($c\Delta H^+$) in coarse mode for different regions. Hyphens indicate the
 439 months when the number counts of trajectories are <10 .
 440

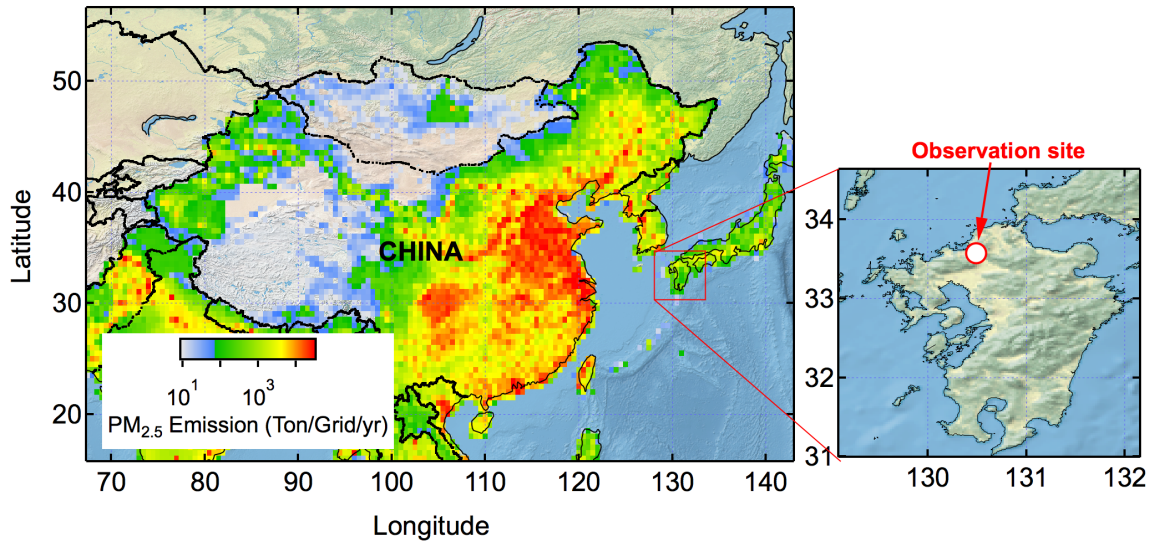
Month (2014)	Region I		Region II		Region III		Region IV	
	Num.	$c\Delta H^+$ (nmol/m ³)	Num.	$c\Delta H^+$ (nmol/m ³)	Num.	$c\Delta H^+$ (nmol/m ³)	Num.	$c\Delta H^+$ (nmol/m ³)
Jan	-	-	203	-5.2 ± 4.5	-	-	-	-
Feb	-	-	108	-5.3 ± 2.4	-	-	-	-
Mar	-	-	114	-1.8 ± 2.6	-	-	-	-
Apr	-	-	175	-3.0 ± 3.4	18	-1.4 ± 2.4	-	-
May	-	-	276	-3.5 ± 6.7	-	-	-	-
Jun	102	3.7 ± 2.5	69	3.4 ± 2.5	-	-	14	13.2 ± 16.7
Jul	34	2.5 ± 1.3	33	4.7 ± 3.1	-	-	85	4.2 ± 3.8
Aug	132	4.8 ± 2.9	-	-	136	1.5 ± 3.1	71	5.1 ± 2.7
Sep	22	2.4 ± 3.6	-	-	104	5.9 ± 2.7	-	-
Oct	26	4.7 ± 3.7	107	1.1 ± 4.3	-	-	-	-
Nov	-	-	629	-1.7 ± 4.4	-	-	-	-
Dec	12	-5.9 ± 1.3	527	-3.7 ± 1.8	-	-	-	-

441

442

List of Figures

443



444

445 Figure 1. Geographic location of the observation site and annual anthropogenic emissions of
446 primary PM_{2.5} in East Asia according to REAS2.0 emission inventory.

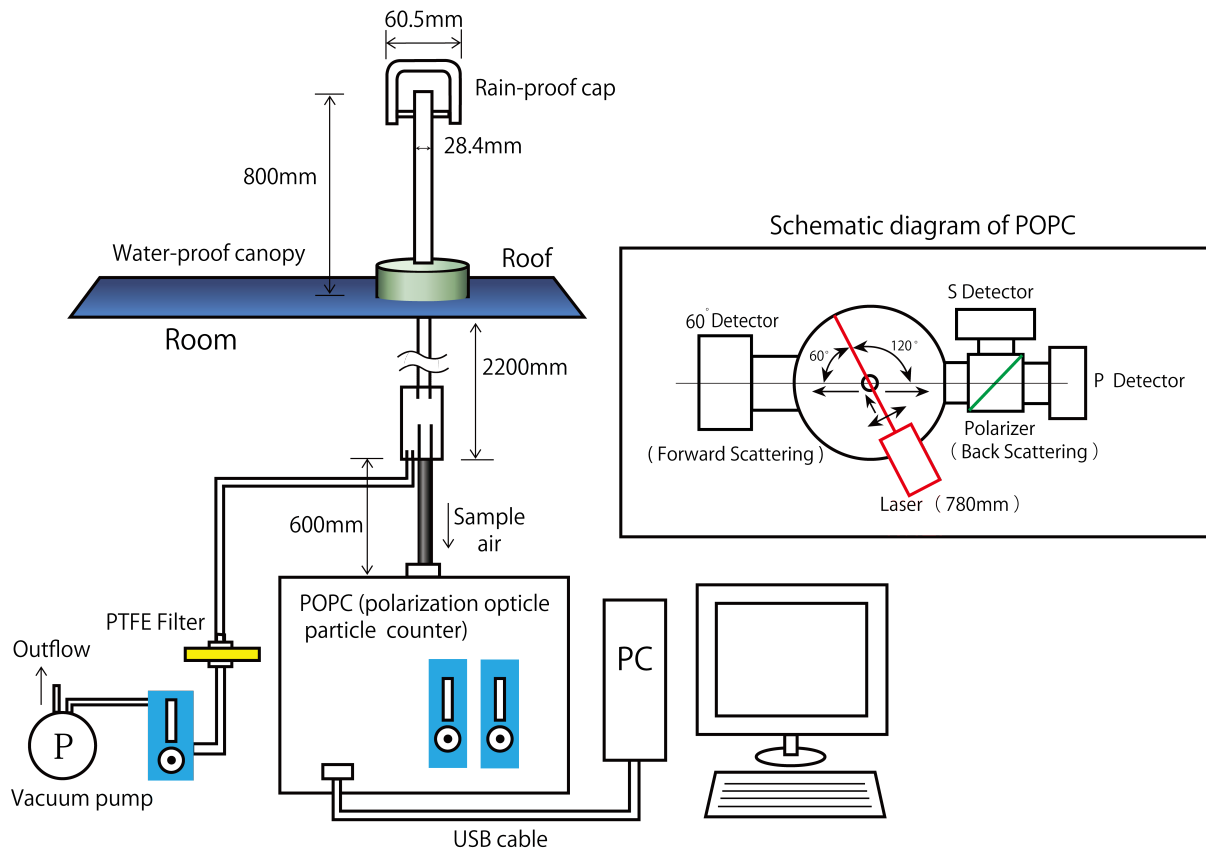
447

448

449

450

451



452

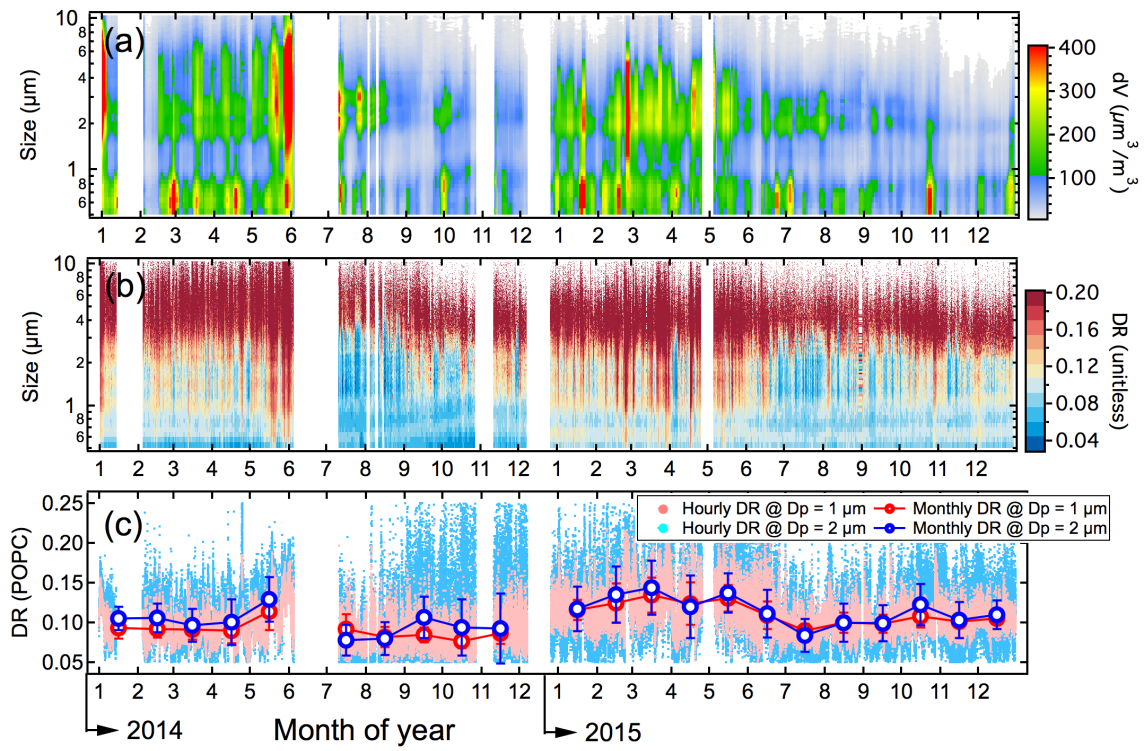
453 Figure 2. The layout of the instrument and schematic diagram of the polarization optical
 454 particle counter (POPC).

455

456

457

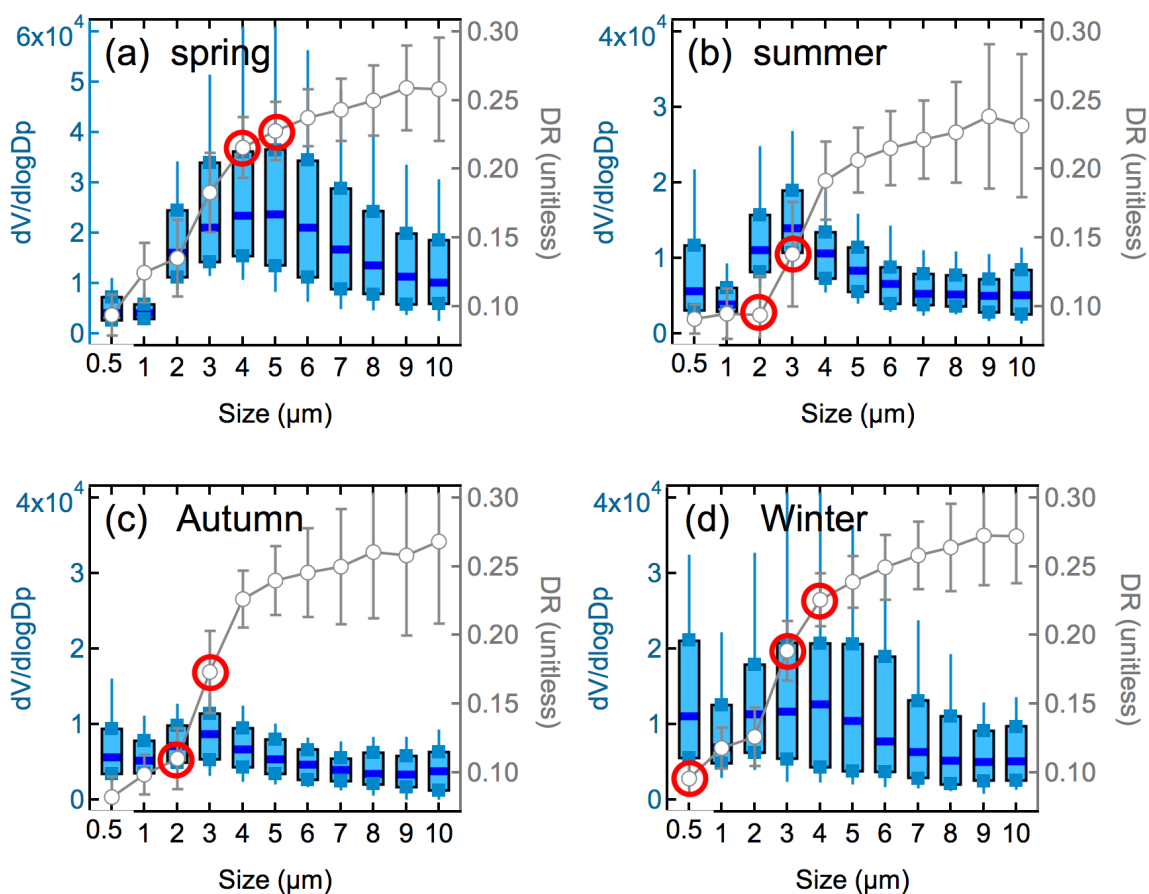
458



459

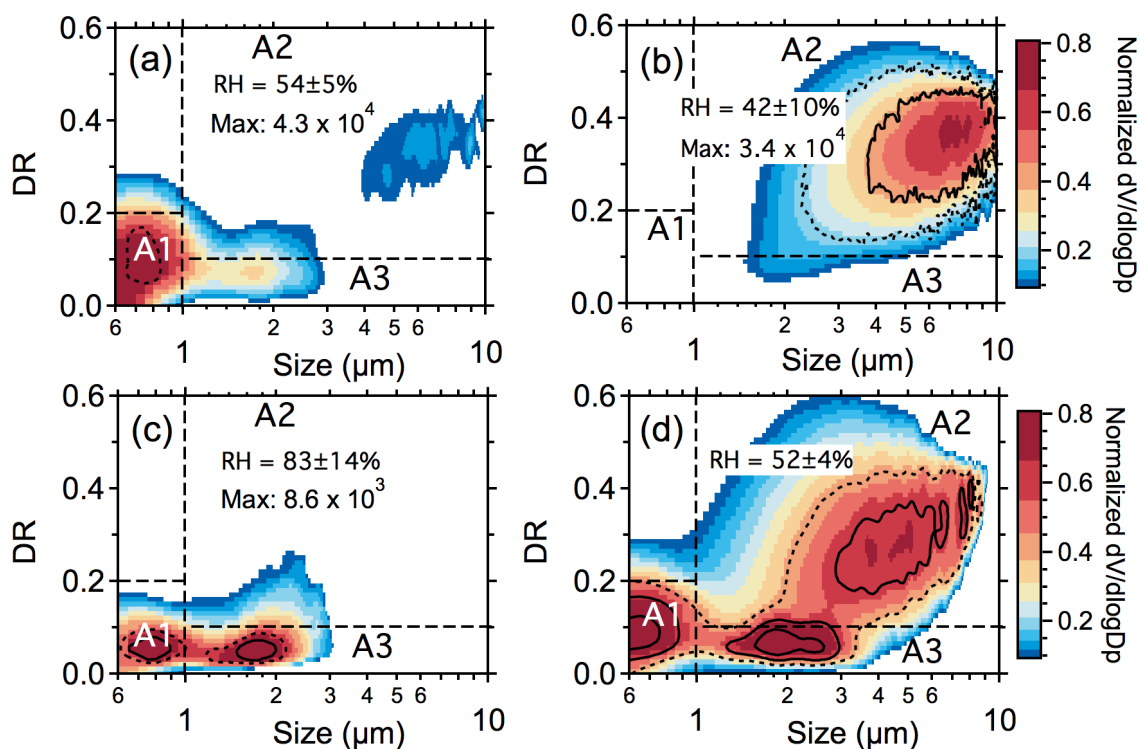
460 Figure 3. Time series of volume size distributions (a), depolarization ratio (b), monthly
 461 averaged depolarization ratio for the particles at $D_p = 1 \mu\text{m}$ and $D_p = 2 \mu\text{m}$ (c) in 2014 and
 462 2015.

463



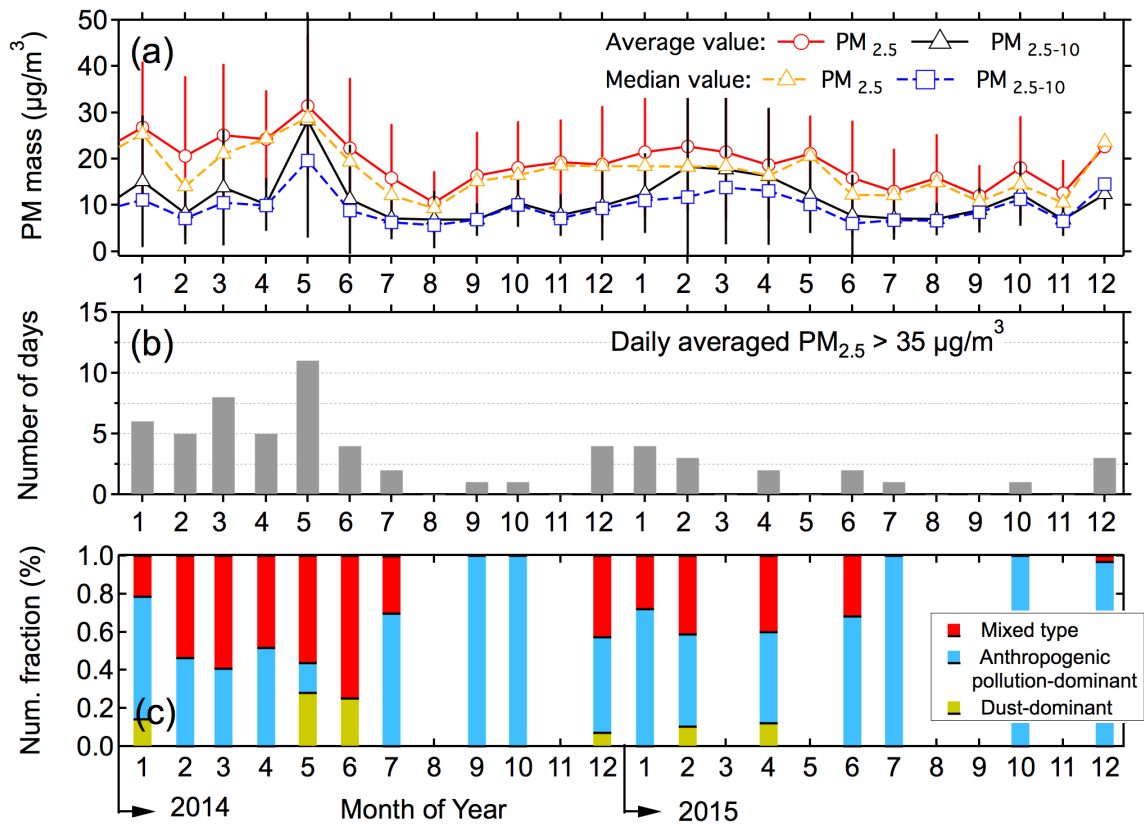
464

465 Figure 4. Volume size distribution (left axis) and size-dependent depolarization ratio (right
 466 axis) of aerosols in (a) spring (March, April, May: MAM), (b) summer (June, July, August:
 467 JJA), (c) autumn (September, October, November: SON), and (d) winter (December, January,
 468 February: DJF). The box and whiskers in the plot represent the 10th, 25th, 75th, 90th
 469 and median values, and the red circles represent the corresponding DR values for the peak
 470 size range in the volume size distribution.



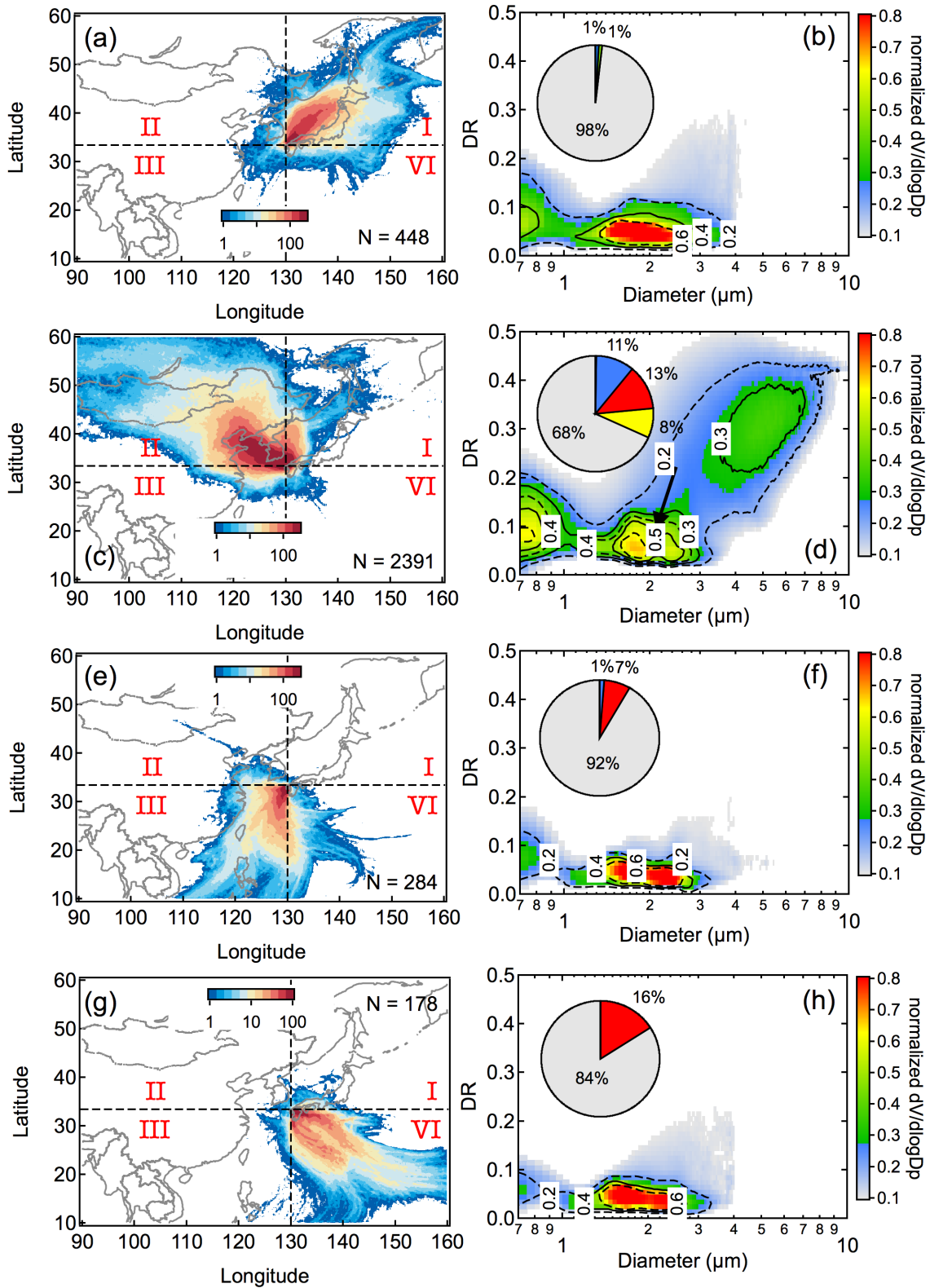
471

472 Figure 5. Variation in the depolarization ratio as a function of particle size for (a)
 473 anthropogenic-pollution-dominant, (b) mineral-dust-dominant, (c) typhoon influenced, and
 474 mixed aerosol types. Colors represent normalized volume concentrations (maximum
 475 value = 1). The relative humidity (RH, from the Japan Meteorological Agency,
 476 <http://www.jma.go.jp/jma/index.html>) values in the plot are the means for each period.



477

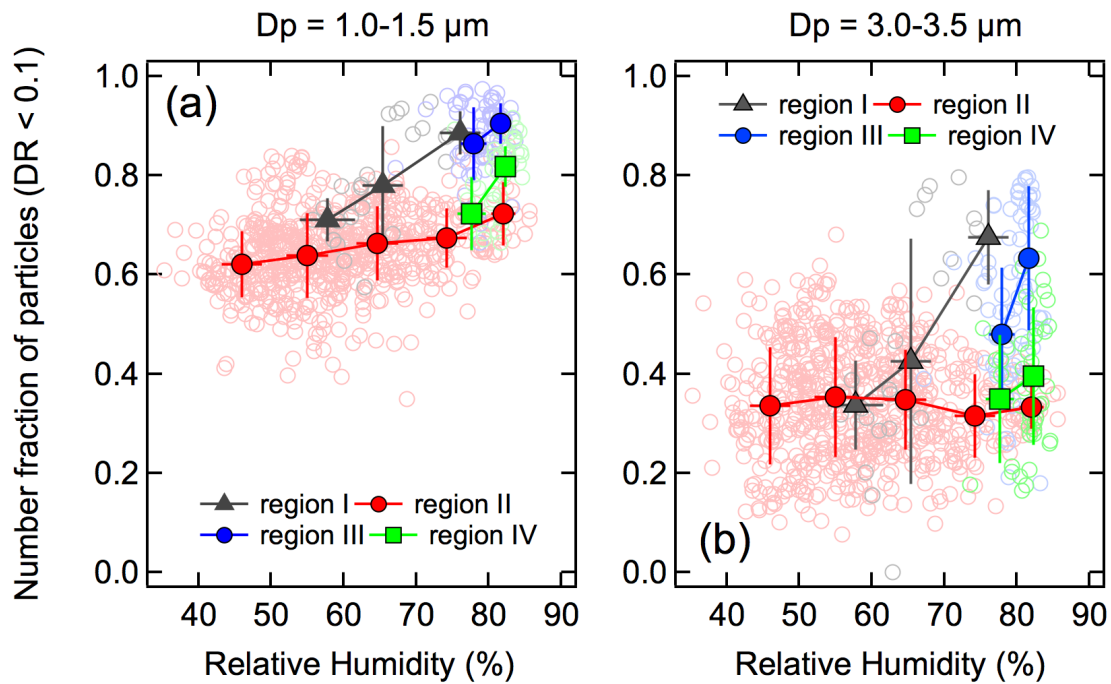
478 Figure 6. (a) The monthly mean and median values of mass concentrations of $PM_{2.5}$ and
 479 $PM_{2.5-10}$, (b) number of days, with daily averaged mass concentrations of $PM_{2.5}$ exceeding 35
 480 $\mu\text{g}/\text{m}^3$ (the National Ambient Air Quality Standard (NAAQS) of $PM_{2.5}$ in Japan), and (c)
 481 contributions of different aerosol types to substandard air quality days at the site during the
 482 observation period.



484

485 Figure 7. Air masses arriving at the observation site, originating from Regions I (a), II (c), III
 486 (e) and Region IV (g). The color scale represents the total number (logarithmic scale) of
 487 trajectories that passed through the mixing layer of the target grid. The N value indicates the
 488 total hours in each scenario, and the total number of trajectories actually is N value multiplied

489 by 27 because ensemble simulations. The corresponding size-resolved depolarization
 490 characteristics of transported particles are shown in (b), (d), (f), and (h). Gray in the pie chart
 491 indicates the number fraction of days that meet the air quality standard. Red, yellow, and blue
 492 indicate the number fractions of substandard air quality days caused by anthropogenic-
 493 pollution-dominant, mineral-dust-dominant, and mixed-type-dominant scenarios,
 494 respectively.
 495



496
 497 Figure 8. Scatter plots of the dependence of the number fraction of particles ($DR < 0.1$) as a
 498 function of relative humidity for different size ranges (a) 1.0-1.5 μm and (b) 3.0-3.5 μm . The
 499 light-colored circles in the background of the plot are the original data used for performing
 500 the statistical analyses.